Physics-based numerical optimization of normally illuminated MUTC photodetectors achieving 50-GHz 3-dB bandwidth

Raonaqul Islam, Curtis R. Menyuk, and Ergun Simsek

University of Maryland Baltimore County
1000 Hilltop Circle, 21250 Baltimore, MD, United States

ABSTRACT

We present a physics-based numerical optimization of a normally illuminated, 14 μm-diameter InGaAs/InP/InGaAsP modified uni-traveling-carrier photodetector that achieves a 3-dB bandwidth of 50 GHz. A particle-swarm optimization framework evaluates 1000 unique layer configurations, each assessed via our in-house drift-diffusion equations solver, using a cost function that maximizes bandwidth. The optimized device's bandwidth decreases by 6 GHz only when the incident power is increased from 10 mW to 200 mW.

Keywords: photodetectors, photoiodes, MUTC, numerical optimization, bandwidth.

1. INTRODUCTION

High-speed photodetectors are a critical enabling technology for microwave photonics, optical frequency comb systems, and ultrabroadband optical communications. In uni-traveling-carrier (UTC) photodetectors[1–4] and their modified versions (MUTC),[5–11] the achievable 3-dB bandwidth is fundamentally constrained by carrier transit time, *RC* parasitics, and space-charge screening. A conventional strategy for pushing bandwidth into the sub-100-GHz regime is aggressive device scaling: reducing the detector diameter lowers capacitance, while thinning the absorption region shortens carrier transit time. As illustrated in Fig. 1(a), shrinking the dimensions from tens of micrometers to a few micrometers can raise the bandwidth from tens of gigahertz to well beyond 200 GHz.[1,4] However, the reduced absorption volume associated with scaling reduces optical absorption, quantum efficiency, and RF output power. Achieving high bandwidth together with moderate quantum efficiency requires careful engineering of the layer structure (thicknesses and doping profiles of the absorption, drift, and charge-compensation layers) rather than relying on geometric scaling alone.

Waveguide-integrated MUTC photodetectors circumvent this trade-off by decoupling the absorption length from the vertical carrier transit distance: optical absorption occurs laterally along the propagation direction, enabling thin absorption regions without sacrificing efficiency, while the elongated junction geometry simultaneously reduces capacitance. Bandwidths approaching or exceeding 200 GHz have been reported in this geometry.[12,13] Nevertheless, top- and bottom-illuminated (normally illuminated) devices remain highly attractive because they offer simpler optical coupling and packaging, compatibility with large-mode-area beams and high-power illumination, mature fabrication processes, and straightforward integration with conventional microwave packaging. These advantages are difficult to replicate in waveguide geometries, which require submicron alignment tolerances and complex heterogeneous integration platforms.

In this work, we address the bandwidth (BW) optimization of normally illuminated MUTC photodetectors through physics-based numerical optimization. Starting from a well-characterized 15-layer InGaAs/InP/InGaAsP baseline (MUTC-16[11]), we employ a particle-swarm optimization (PSO) framework[14] to explore the high-dimensional space of layer thicknesses and doping concentrations. The cost function is set to $(\mathrm{BW})^{-1}$, directly rewarding higher 3-dB bandwidth. Targeting a fixed device diameter of 14 μm, a practical size for normal-incidence operation, we evaluate 1000 unique designs and identify an optimized device with a 3-dB bandwidth of 50 GHz.

Further author information: (Send correspondence to E. S.)
E-mail: simsek@umbc.edu, Telephone: +1 (410) 455 3540

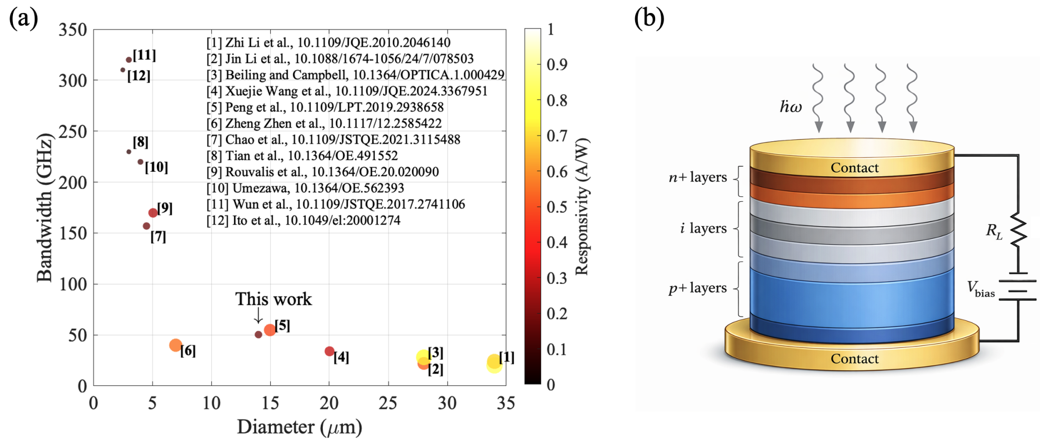

Figure 1: (a) Compiled literature data showing the bandwidth–diameter trade-off. Circle size and color indicate increasing responsivity. (b) Schematic of a reverse-biased photodetector illuminated from its n-side; thin yellow layers represent the ohmic contacts.

2. DRIFT-DIFFUSION SOLVER AND MATERIAL MODELING

Figure 1(b) illustrates the configuration studied in this work: a reverse-biased photodetector illuminated through the n-side contact. Our drift-diffusion equation solver (DDES) is based on the electron and hole continuity equations coupled to Poisson's equation:

$$\frac{\partial(p - N_A^-)}{\partial t} = -\frac{1}{q}\nabla \cdot \mathbf{J}_p + G_{\text{ii}} + G_{\text{opt}} - R(n,p), \tag{1a}$$

$$\frac{\partial(n - N_D^+)}{\partial t} = +\frac{1}{q}\nabla \cdot \mathbf{J}_n + G_{\text{ii}} + G_{\text{opt}} - R(n,p), \tag{1b}$$

$$\nabla \cdot \mathbf{E} = \frac{q}{\epsilon}\left(n - p + N_A^- - N_D^+\right), \tag{1c}$$

where n and p are the electron and hole densities; t is time; q is the elementary charge; $\mathbf{J}_n$ and $\mathbf{J}_p$ are the electron and hole current densities; R is the net recombination rate; G_{ii} and G_{opt} are the impact-ionization and optical generation rates, respectively; $\mathbf{E}$ is the electric field; ϵ is the permittivity; and N_A^-, N_D^+ are the ionized acceptor and donor concentrations. The complete formulation and all material parameters are detailed in our earlier work.[15]

The solver incorporates material-specific models for all constituent III–V semiconductors. Electron and hole mobilities are described by temperature-dependent power-law expressions calibrated to experiment for GaAs, InAs, InP, InGaAs, and InGaAsP, with alloy mobilities obtained from composition-weighted mixing rules. High-field transport is captured through material- and temperature-dependent saturation velocities with non-linear interpolation for ternary and quaternary alloys. Optical generation uses wavelength- and material-dependent absorption coefficients. Bandgap energies are temperature-dependent and include bandgap narrowing as a function of doping and dopant type. Recombination accounts for Shockley–Read–Hall, radiative, and Auger processes. Incomplete dopant ionization is modeled through species-dependent ionization energies. Three numerical features are essential for high efficiency: (i) a non-uniform spatial mesh[16] that concentrates grid points near heterojunction interfaces for stability; (ii) non-uniform time-stepping[17] that decreases Δt as we get closer to the peak pulse intensity and increases it back after passing the peak; and (iii) a broadband windowing-function technique[15] that extracts the full RF output power spectrum from a single time-domain simulation.

The MUTC-16 photodiode, originally designed, fabricated, and characterized by Beling and Campbell,[11] serves as the starting point for our optimization. Its 15-layer epitaxial structure has a total thickness of approximately 2.6 μm and a device diameter of 26 μm. From top (p-side) to bottom (n-side), the structure is as follows. The p-type contact is a 50 nm InGaAs layer doped at 2.0×10^{19} cm^{-3} (Zn). A 100 nm InP cap layer at 2.0×10^{18} cm^{-3} suppresses electron back-diffusion into the contact. Two InGaAsP grading layers (Q1.1 and Q1.4, 15 nm each) smooth the valence-band discontinuity at the InP/InGaAs interface. The graded p-doped absorber comprises three InGaAs layers (120, 180, and 180 nm at 5.0×10^{18}, 1.3×10^{18}, and 4.0×10^{17} cm^{-3}, respectively); the decreasing doping profile creates a quasi-field that accelerates holes across the undepleted absorber. A lightly doped n-type InGaAs layer (160 nm, 1.0×10^{16} cm^{-3}) forms the upper portion of the depletion region, followed by two n-type InGaAsP grading layers. A moderately doped InP cliff layer (50 nm, 1.9×10^{17} cm^{-3}) shapes the electric field profile in the collector. Two lightly doped InP collector layers reduce junction capacitance, and the structure is completed by two heavily doped InP sub-contact layers that minimize contact resistance.

3. NUMERICAL RESULTS

All simulations use continuous-wave illumination at 1550 nm modulated by a broadband RF signal. The device diameter is fixed at 14 μm and the load resistance at 50 Ω. The maximum mesh spacing is 0.5 nm, the Blackman–Harris windowing function cutoff is 100 GHz, and the time-step is 0.1 ps. For the electric-field and RF bandwidth comparisons, the bias voltage is $V_{\text{bias}} = -5$ V and the incident power is 10 mW; sensitivity to the bias voltage and incident power is examined separately below.

The PSO algorithm[14] explored the 30-dimensional space of layer thicknesses and doping concentrations simultaneously. Thicknesses were bounded to $[15, 1500]$ nm (integer values); doping concentrations were bounded to $[10^{15}, 10^{20}]$ cm^{-3} (two significant figures). Using 20 particles (swarms) and iterating until 1000 unique designs were generated, each evaluated via our in-house drift-diffusion equations solver,[15,16] the optimizer minimized the cost function $\mathcal{C} = 1/\text{BW}$, directly maximizing the 3-dB bandwidth. Table 1 lists the layer parameters of the best design together with the tolerable variation of each parameter that achieved comparable performance during the PSO search, providing practical fabrication windows.

Table 1: Layer structures of the MUTC-16 baseline and the optimized design. The "tolerance" columns list the tolerable changes observed among designs that achieved comparable performance during the PSO search, providing a fabrication tolerance window.

Type	Material	MUTC-16		Optimized Design			
		Thickness (nm)	Doping (cm^{-3})	Thickness (nm)		Doping (cm^{-3})	
				Best	Tolerance	Best	Tolerance
p	InGaAs	50	2.00×10^{19}	20	± 2	8.00×10^{19}	$\pm 0.50 \times 10^{19}$
p	InP	100	2.00×10^{18}	100	± 5	1.00×10^{19}	$\pm 0.10 \times 10^{19}$
p	InGaAsP (Q1.1)	15	5.00×10^{18}	10	± 1	3.00×10^{18}	$\pm 0.10 \times 10^{18}$
p	InGaAsP (Q1.4)	15	5.00×10^{18}	100	± 5	1.10×10^{17}	$\pm 0.10 \times 10^{17}$
p	InGaAs	120	5.00×10^{18}	95	± 5	1.02×10^{16}	$\pm 2.00 \times 10^{15}$
p	InGaAs	180	1.30×10^{18}	85	± 5	1.02×10^{16}	$\pm 2.00 \times 10^{15}$
p	InGaAs	180	4.00×10^{17}	30	± 2	2.34×10^{17}	$\pm 0.20 \times 10^{17}$
n	InGaAs	160	1.00×10^{16}	30	± 2	1.01×10^{15}	$\pm 0.06 \times 10^{15}$
n	InGaAsP (Q1.4)	15	1.00×10^{16}	30	± 5	1.01×10^{17}	$\pm 1.20 \times 10^{16}$
n	InGaAsP (Q1.1)	15	1.00×10^{16}	100	± 5	1.38×10^{17}	$\pm 0.30 \times 10^{17}$
n	InP	50	1.90×10^{17}	100	± 5	1.01×10^{16}	$\pm 0.01 \times 10^{16}$
n	InP	300	1.50×10^{16}	200	± 6	9.23×10^{16}	$\pm 0.43 \times 10^{16}$
n	InP	440	1.20×10^{16}	100	± 2	1.01×10^{17}	$\pm 0.10 \times 10^{17}$
n	InP	100	1.00×10^{18}	500	± 8	4.10×10^{18}	$\pm 0.50 \times 10^{18}$
n	InP	900	1.00×10^{19}	1000	± 50	9.90×10^{19}	$\pm 0.10 \times 10^{19}$

Figure 2 summarizes the 1000 evaluated designs in the bandwidth–quantum efficiency plane, with marker color encoding the intrinsic-region thickness (t_i). The scatter reveals the fundamental tension between bandwidth and quantum efficiency: designs with high QE tend to have thicker absorption regions (lighter markers), which increases transit time and reduces bandwidth. The optimized design, with QE = 0.14 and BW = 50 GHz, lies in the high-bandwidth, low-QE region of the trade-off frontier. Thinner intrinsic regions (darker markers) are associated with the highest bandwidths but the lowest efficiencies, confirming that the PSO, guided by the 1/BW cost function, systematically drove toward compact, fast-transit designs.

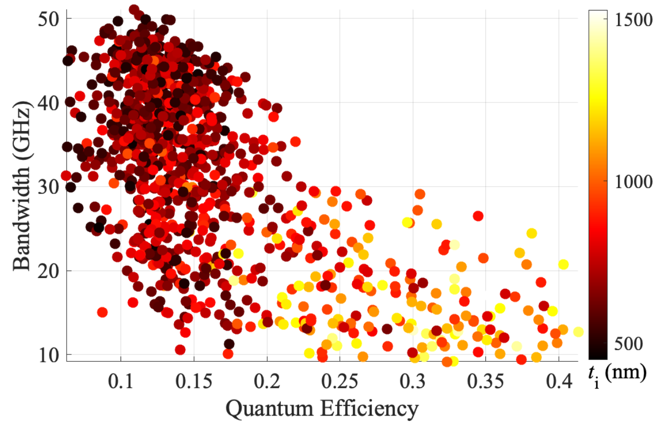

Figure 2: Bandwidth vs. quantum efficiency for the 1000 evaluated designs. Marker color encodes the intrinsic-region thickness (t_i). High-bandwidth designs cluster at low QE and small t_i, illustrating the bandwidth–efficiency trade-off.

Figure 3 compares the electric field magnitude profiles of the MUTC-16 and the optimized design at $V_{\text{bias}} = -5$ V and 10 mW incident power. The optimized design has a depletion region that extends much farther into the absorber than the baseline device, which is expected to improve carrier transit time while still maintaining the MUTC concept. In the optimized design, the primary depletion peak is narrower compared to MUTC-16's and concentrated near 0.5 μm with a peak field of approximately 205 kV/cm. Concentrating the applied bias over a thinner, higher-field depletion region drives carriers closer to their saturation velocity throughout the sweep-out path, reducing transit time and suppressing the low-field diffusive tail that limits bandwidth in thicker structures. The secondary field peaks in the collector further accelerate electrons toward the n-contact, minimizing the slow-carrier accumulation that would otherwise degrade high-frequency response.

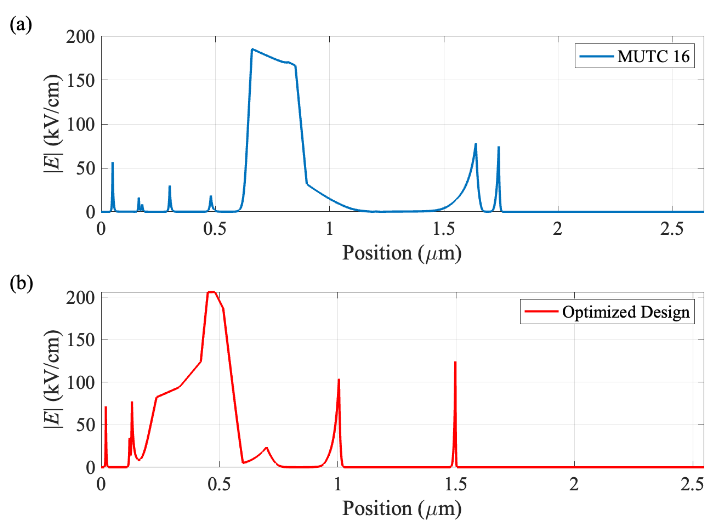

Figure 3: Electric field magnitude along (a) the MUTC-16 and (b) the optimized design at $V_{\text{bias}} = -5$ V and $P_{\text{inc}} = 10$ mW. The optimized design features a compressed primary depletion peak and engineered secondary peaks in the collector region.

Figures 4 (a) and (b) show the total (I), electron (I_n), hole (I_p), and displacement (I_d) currents as a function of time for MUTC-16 and optimized design, respectively. For both designs, the dominant component is the electron current as expected. The optimized design's output current is 2.3 times smaller than the MUTC-16's. This is also reflected in their quantum efficiencies, i.e., optimized design's $Q_{\text{eff}} = 0.14$ and MUTC's $Q_{\text{eff}} = 0.30$.

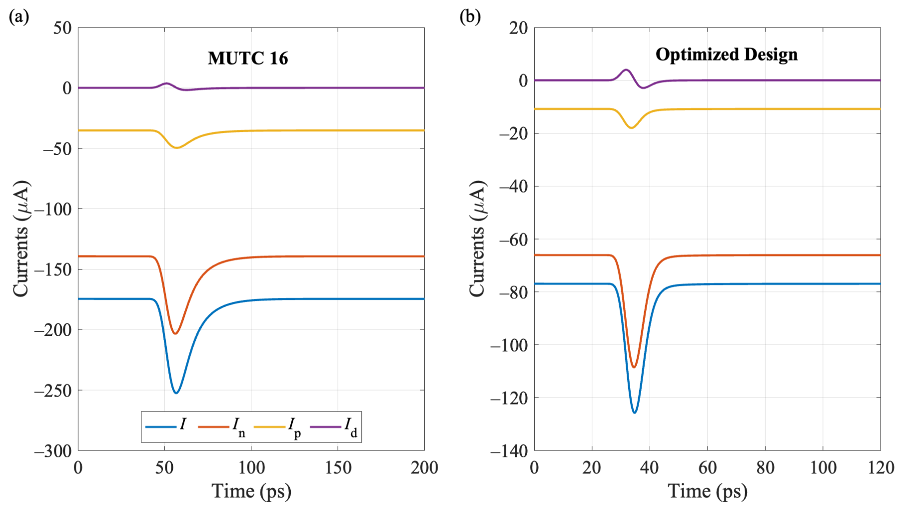

Figure 4: Total (I), electron (I_n), hole (I_p), and displacement (I_d) currents as a function of time for MUTC 16 and optimized design as a function of time. The broadband excitation starts at one fourth of the total simulation time.

Figure 5 shows the normalized RF output power as a function of modulation frequency. The MUTC-16 exhibits a 3-dB bandwidth of 15.6 GHz, while the optimized design achieves 50 GHz, a 3.2× improvement. The roll-off of the optimized design is smooth and monotonic up to 70 GHz, with no resonance peaks or gain ripple, confirming that the bandwidth enhancement arises from genuine improvement of the internal carrier dynamics rather than from impedance resonances or partial cancellation artifacts. The responsivity of the optimized design is 0.17 A/W.

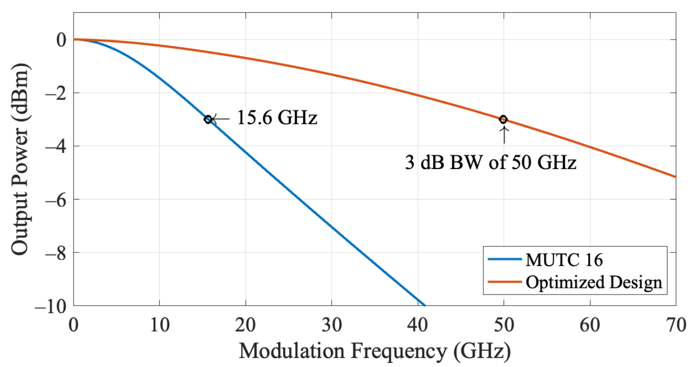

Figure 5: Normalized RF output power vs. modulation frequency. The 3-dB bandwidths are 15.6 GHz (MUTC-16) and 50 GHz (optimized design).

Figure 6 shows the 3-dB bandwidth of the optimized design as a function of incident optical power for five reverse bias voltages from −2 V to −6 V. Two trends are immediately apparent. First, bandwidth increases monotonically with reverse bias at all incident power levels. At low incident power (10 mW), increasing the bias from −2 V to −6 V raises the bandwidth from approximately 35 GHz to 51 GHz. This behavior is expected: a larger reverse bias extends and intensifies the depletion field, driving carriers more uniformly to their saturation velocity and reducing the transit-time contribution to bandwidth. Second, at a fixed bias below −2 V, the bandwidth decreases as the incident power increases from 10 mW to 200 mW. This degradation is a signature of space-charge screening: the photogenerated electron-hole plasma partially collapses the internal electric field, reducing carrier velocities and increasing the effective transit time. The effect is most severe at lower biases , where the bandwidth drops to 10-12 GHz at 200 mW, reflecting the vulnerability of shallow depletion fields to screening. At −6 V the bandwidth remains above 44 GHz across the full power range, indicating that higher reverse bias provides a useful degree of protection against space-charge saturation.

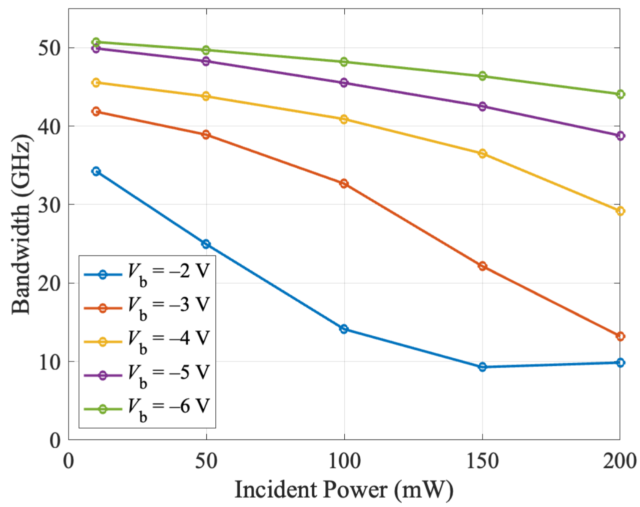

Figure 6: 3-dB bandwidth of the optimized design as a function of incident power for bias voltages from −2 V to −6 V. Bandwidth increases with reverse bias and decreases with increasing incident power.

Saturation behavior and output power optimization were not included in the present cost function and will be the subject of future work. We plan to extend the framework to simultaneous optimization of bandwidth and saturation current for high-dynamic-range microwave photonics applications.

4. CONCLUSION

We have demonstrated physics-based numerical optimization of a normally illuminated 14-μm-diameter InGaAs/InP/InGaAsP MUTC photodetector using a particle-swarm optimization framework that evaluated 1000 unique designs by numerically solving the drift-diffusion equations. The optimized device achieves a 3-dB bandwidth of 50 GHz with a quantum efficiency of 0.14 and a responsivity of 0.17 A/W. The bandwidth improvement is attributed to a compressed primary depletion region with a higher peak field and engineered secondary collector peaks that maintain near-saturation carrier velocities throughout the device. Bandwidth increases with reverse bias voltage and is moderately degraded by space-charge screening at high incident powers, with the −6 V bias case retaining greater than 44 GHz bandwidth up to 200 mW. The optimized layer parameters and their tolerable bounds provide practical design windows for fabrication of next-generation top-illuminated MUTC photodetectors.

REFERENCES

[1] Ito, H., Furuta, T., Kodama, S., and Ishibashi, T., "InP/InGaAs uni-travelling-carrier photodiode with 310 GHz bandwidth," *Electronics Letters* **36**(21), 1809–1810 (2000).

[2] Rouvalis, E., Chtioui, M., van Dijk, F., Lelarge, F., Fice, M. J., Renaud, C. C., Carpintero, G., and Seeds, A. J., "170 GHz uni-traveling carrier photodiodes for InP-based photonic integrated circuits," *Opt. Express* **20**, 20090–20095 (Aug 2012).

[3] Wun, J.-M., Wang, Y.-W., and Shi, J.-W., "Ultrafast uni-traveling carrier photodiodes with $GaAs_{0.5}Sb_{0.5}/In_{0.53}Ga_{0.47}$as type-ii hybrid absorbers for high-power operation at THz frequencies," *IEEE Journal of Selected Topics in Quantum Electronics* **24**(2), 1–7 (2018).

[4] Umezawa, T., Nakajima, S., Matsumoto, A., Akahane, K., and Yamamoto, N., "DC-220 GHz well-impedance matched ultra-broadband photodetector for high symbol rate advanced optical fiber communication," *Opt. Express* **33**, 25325–25338 (Jun 2025).

[5] Li, J., Xiong, B., Sun, C., Miao, D., and Luo, Y., "Analysis of frequency response of high power MUTC photodiodes based on photocurrent-dependent equivalent circuit model," *Opt. Express* **23**, 21615–21623 (Aug 2015).

[6] Li, J., Xiong, B., Sun, C.-Z., Luo, Y., Wang, J., Hao, Z.-B., Han, Y.-J., Wang, L., and Li, H.-T., "Bandwidth improvement of high power uni-traveling-carrier photodiodes by reducing the series resistance and capacitance," *Chinese Physics B* **24**, 078503 (may 2015).

[7] Estrella, S., Johansson, L. A., Mashanovitch, M. L., and Beling, A., "High-power MUTC photodetectors for RF photonic links," in [*Terahertz, RF, Millimeter, and Submillimeter-Wave Technology and Applications IX*], **9747**, 97471X, SPIE (2016).

[8] Zhen, Z., Hao, R., Xing, D., Feng, Z., Jin, S., and Li, E., "Back-illuminated modified uni-traveling-carrier photo-diodes (MUTC-PDs) with 3-dB bandwidth over 40 GHz," in [*International Conference on Optoelectronic and Microelectronic Technology and Application*], **11617**, 1161731, SPIE (2020).

[9] Tian, Y., Xiong, B., Sun, C., Hao, Z., Wang, J., Wang, L., Han, Y., Li, H., Gan, L., and Luo, Y., "Ultrafast MUTC photodiodes over 200 GHz with high saturation power," *Opt. Express* **31**, 23790–23800 (Jul 2023).

[10] Wang, X., Huang, Y., Tan, S., Du, J., Yang, M., Liu, K., Duan, X., and Ren, X., "Bandwidth optimization and fabrication of high-power MUTC-pd," *IEEE Journal of Quantum Electronics* **60**(2), 1–6 (2024).

[11] Yang, Z., Yu, Q., Zang, J., Campbell, J. C., and Beling, A., "Phase-modulated analog photonic link with a high-power high-linearity photodiode," *Journal of Lightwave Technology* **36**(18), 3805–3814 (2018).

[12] Li, L., Wang, L., Long, T., Zhang, Z., Lu, J., and Chen, B., "Ultra-fast waveguide MUTC photodiodes over 220 GHz," *Journal of Lightwave Technology* **42**(21), 7451–7457 (2024).

[13] Li, L., Long, T., Yang, X., Zhang, Z., Wang, L., Wang, J., Wang, M., Lu, J., Yu, J., and Chen, B., "Modified uni-travelling-carrier photodiodes with 206 GHz bandwidth and 0.81 A/W external responsivity," *Nature Photonics* **19**(12), 1301–1308 (2025).

[14] Anjum, I. M., Simsek, E., Mahabadi, S. E. J., Carruthers, T. F., Menyuk, C. R., Campbell, J. C., Tulchinsky, D. A., and Williams, K. J., "Use of evolutionary optimization algorithms for the design and analysis of low bias, low phase noise photodetectors," *Journal of Lightwave Technology* **41**(23), 7285–7291 (2023).

[15] Simsek, E., Anjum, I. M., Carruthers, T. F., Menyuk, C. R., Campbell, J. C., Tulchinsky, D. A., and Williams, K. J., "Fast evaluation of RF power spectrum of photodetectors with windowing functions," *IEEE Transactions on Electron Devices* **70**(7), 3643–3648 (2023).

[16] Simsek, E., Anjum, I. M., and Menyuk, C. R., "Solving drift diffusion equations on non-uniform spatial and temporal domains," in [*44th PhotonIcs & Electromagnetics Research Symposium (PIERS)*], (July 2023).

[17] Simsek, E., Anjum, I. M., Carruthers, T. F., and Menyuk, C. R., "Non-uniform time-stepping for fast simulation of photodetectors under high-peak-power, ultra-short optical pulses," in [*2022 International Conference on Numerical Simulation of Optoelectronic Devices (NUSOD)*], 1–2 (2022).